Nonlinear dynamics of an acoustically compact orifice

Author(s):
Stoychev, Alexander K.; Noiray, Nicolas

Publication date:
2024-12-22

Permanent link:
https://doi.org/https://doi.org/10.3929/ethz-b-000692623

Originally published in:
Journal of Sound and Vibration 593, https://doi.org/10.1016/j.jsv.2024.118660

Journal of Sound and Vibration 593 (2024) 118660

Contents lists available at ScienceDirect

Journal of Sound and Vibration

journal homepage: www.elsevier.com/locate/jsvi

Nonlinear dynamics of an acoustically compact orifice

Alexander K. Stoychev *, Nicolas Noiray *

CAPS Laboratory, Department of Mechanical and Process Engineering, ETH Zürich, 8092, Zürich, Switzerland

ARTICLE INFO

Keywords:
Acoustics
Aeroacoustics
Nonlinear dynamical systems
Reduced order modeling

ABSTRACT

This work presents a three dimensional, reduced order model of the dynamics of an acoustically compact aperture, subject to an arbitrary pressure forcing. It provides the time evolution of the velocity profile across the orifice section as function of the dynamical pressure excitation. The volume flow can be deduced therefrom, and can thus provide predictions of the fundamental frequency based orifice impedance. The representation of the nonlinear aperture flow proposed here establishes a direct mathematical relation to the fundamental equations of fluid mechanics. This offers a better understanding of the dominant physical mechanisms governing the system's dynamics and allows for good *a priori* estimates without supporting experiments. The model assumes that the viscosity induced rotational component of the fluid motion can be reduced to a discontinuity at the in-flow plane of the thin orifice, without significantly influencing the normal velocity profile. This seemingly unconventional assumption is solely targeting the acoustics problem and is validated with direct numerical simulations (DNS) of the aperture flow, using a compressible solver of the Navier–Stokes equations. Apart from the DNS, the model predictions are also validated against well established experimental results from the literature.

1. Introduction

The dynamics of an acoustically compact aperture has a long history of extensive study, reaching as far back as the seminal work on sound in [1]. Apart from earlier developments on the linear acoustics of the problem [e.g. 2], a substantial amount of research effort has been devoted to experimental and theoretical investigations of the prominent nonlinear effects observed at higher acoustic forcing amplitudes (see e.g. [3–12] for a survey).

As first experimentally observed in [3], the pressure transmitted through, and by extension, the average velocity in, a compact aperture ceases to be directly proportional to the forcing amplitude at high sound pressure levels (SPLs), indicating nonlinear behavior. In particular, the conclusion was reached that the amplitude of the forcing pressure seems to be roughly proportional to the square of the average fluid velocity over the aperture. This conjecture was later confirmed by numerous other experimental studies [e.g. 4–6,8], while the thorough investigation of [7] showed, by means of hot wire anemometer measurements, that for the total velocity at the center of the aperture this proportionality factor is approximately equal to the fluid density. In good approximation, this statement holds true for a wide variety of different media, e.g. air [4,5,7]; water [6] and oil [13].

Based on this influential body of research, several models aiming at describing the aperture dynamics have been proposed, ranging from simple empirical formulas accompanying the experimental data of [3,6,7], to the more advanced fluid mechanical models of [9–11,14–16]. Furthermore, the latter works apply a wide variety of modeling techniques, extending from the 1D models of [9,10], employing empirical parameters and piecewise approximations in the "linear" and "nonlinear" regime, respectively, to analytical discrete vortex [11,14,15] and viscous [16] models. Additionally, a linear 3D model of the dynamics of an acoustically

* Corresponding author.
E-mail addresses: astoychev@ethz.ch (A.K. Stoychev), noirayn@ethz.ch (N. Noiray).

https://doi.org/10.1016/j.jsv.2024.118660
Received 1 March 2024; Received in revised form 28 July 2024; Accepted 5 August 2024
Available online 6 August 2024

compact aperture in an infinite rigid wall, based on incompressibility and irrotationality assumptions, has been derived from first principles in [17, pp. 354–360]. It represents a fluid mechanical analogy to the classical problem of the uniformly electrified disc [cf. 18] and offers a significant improvement in the understanding of the linear problem by providing a detailed linear approximation of both the space and time behavior of the system.

The assumption of an irrotational flow in each of the half spaces seems severely limiting in light of the experimental work presented in [19] and to a some extend — the theoretical developments of [20–22]. The former conducts acoustic measurements and flow visualizations on a wide variety of geometries and flow conditions, including the case of an orifice without mean flow, and discovers a number of similarities. Based thereon, the conclusion is reached, that the observed acoustic losses might be well explained by the aforementioned theoretical work pertaining to the bias flow case, where the vortex shedding and convection is the main contributor to the acoustic losses. This should be, at least to a certain extend, also true in the no mean flow environment, yet resting on experimental measurements and theoretical analysis [10, sec. V] hypothesizes that if global quantities like mass flow through the aperture or analogously, the velocity profile at the in-flow plane are sought, some significant simplifications can be made. In particular, based on empirical evidence, albeit surprisingly, [10, sec. V] concludes that ignoring the complicated details of vortex shedding from the edge of the aperture proves to be a successful design strategy for the zero mean flow problem. Specifically, those modeling efforts establish that reduced order representations, completely ignoring the vortex dynamics and only exhibiting the effects of tangential velocity jump at the aperture plane, are fully capable of reproducing experimental measurements within good accuracy. Furthermore, numerical vortex shedding simulations [23] and the simplified discrete vortex models [11] also show that even when the vortex motion is considered carefully, seemingly important details like the path along which the vortex ring travels prove to be practically irrelevant for the resulting orifice velocity [cf. 11, fig. 11–13]. In fact the vortex sheet induced irrotational field they are calculating seems to be the relevant quantity. Additionally, earlier developments [9] based on the yet another different assumption of 3D spherical flow also lead to reasonable approximations of the forced aperture behavior as measured in [6,7], despite the authors' well founded argument [9, section 2.1.1] that the aforementioned assumptions could only be approximately valid on the in-flow side of the orifice. The analysis of the experimental findings of [6–8] conducted in [9, p. 34] is also worth considering here, since it establishes a quasi-static behavior of the aperture at large forcing amplitudes, where the rather dynamic nature of the vortex motions reported in [cf. 23, fig. 4] would otherwise be expected to strongly affect the mass flow. Furthermore, since experiments on wide variety of different media, e.g. air [7], water [6], oil [13], show essentially identical behavior [see 12, for survey] one could reason that viscosity is not a crucial quantity.

The above observations lend credibility, or at least plausibility, to the [10, sec. V] conjecture that the nonuniform acceleration of the fluid into the orifice due to a uniform pressure forcing is weakly influenced by the specific details of vortex shedding and the latter can be simplified. Inspired by those developments, we adopt the rather unintuitive assumption of irrotationality within the two (separate) half spaces [17, pp. 354–360] and tangential velocity jump at the aperture plane, roughly accounting for vorticity effects. This allows us to adopt the powerful Green's function approach, commonly applied to various problems throughout the aeroacoustics [24] and thermoacoustics community [25–27]. Also note that the aforementioned approach of localizing vorticity at the aperture plane is successfully applied to the generalized case of a (nonlinear) aperture under grazing flow [28].

The main part of this contribution begins with Section 2, where a 3D fluid mechanical model of an acoustically compact aperture in an infinite rigid wall is developed. The model is mathematically coherent and derived from fundamental laws under the potential flow assumptions inside the two (separate) half spaces, mostly based on the general strategy employed in [17, pp. 354–360] or [24–27], however, starting from the nonlinear Navier–Stokes equation and aiming at more accurately representing the dynamics of the aperture flow, as inspired by the work in [9,10]. This eliminates the need of modeling shortcuts like empirical parameters, uniform velocity assumptions or piecewise approximations as employed by the latter two, while still accounting for the most relevant nonlinear effects. This offers both, insight into the dominant physics of the problem and a good accuracy, as illustrated in Section 3 by validation of the model predictions against established experimental results from [7,10], as well as direct numerical simulation performed for the occasion. Specifically, Section 3.1 utilizes the hot wire anemometer measurements of [7] to validate the predictions of the velocity amplitude and phase at the center of the aperture, while in Section 3.2 the transients and steady state of the average dynamics are explored through comparison with the transmitted pressure measurements in [10]. Subsequently, Section 3.3 examines the spatial–temporal behavior of the proposed reduced order representation in greater depth by means of detailed DNS, further assessing the plausibility of the aforementioned assumptions, on which the former rests. After demonstrating the model effectiveness in estimating both general trends and specific values, and applying it to some outstanding questions in Section 3.4, the manuscript concludes with an overview of the results derived therefrom in Section 4.

2. Aperture model

Based on Ingard & Ising's experimental observations of marked changes in the near aperture fluid velocity, over very short distances compared to the sound wavelength [7, fig. 4], it can be concluded [9, p. 9] that the dominant physical mechanism behind the aperture flow is likely to be of hydrodynamic, rather than acoustic nature and that the near field extends to only several aperture diameters. Following their deduction, further verified by the experiments of [11], we assume incompressibility in the near field, which simplifies the continuity equation to

$$\boldsymbol{\nabla} \cdot \boldsymbol{u} = 0, \tag{1}$$

where $\boldsymbol{\nabla} \cdot (\cdot)$ denotes the divergence and $\boldsymbol{u}$ is the velocity vector. Conversely, the Navier–Stokes equation becomes

$$\frac{\partial \boldsymbol{u}}{\partial t} + (\boldsymbol{u} \cdot \boldsymbol{\nabla})\, \boldsymbol{u} = -\frac{\boldsymbol{\nabla} p}{\rho_0} + \nu \boldsymbol{\nabla}^2 \boldsymbol{u}, \tag{2}$$

where $\boldsymbol{\nabla}(\cdot)$ denotes the gradient, $\partial(\cdot)/\partial t$ is the time derivative, ρ_0 is the fluid density, p is the pressure and ν is the kinematic viscosity. Resting on the experimental evidence [10] discussed in Section 1, that in the zero-mean flow case the details of vorticity can be simplified (in contrast to the bias flow case [19,21]), we further assume irrotational flow within the two (separate) half spaces (i.e. $\boldsymbol{\nabla}\times\boldsymbol{u}=\mathbf{0}$) and allow for a tangential velocity jump at the aperture to roughly account for vorticity effects. Recalling the form of the vector Laplacian, $\boldsymbol{\nabla}^2\boldsymbol{u}=\boldsymbol{\nabla}(\boldsymbol{\nabla}\cdot\boldsymbol{u})-\boldsymbol{\nabla}\times(\boldsymbol{\nabla}\times\boldsymbol{u})$, simplifies (2) to the Euler equation

$$\frac{\partial \boldsymbol{u}}{\partial t}+\frac{1}{2}\boldsymbol{\nabla}(\boldsymbol{u}\cdot\boldsymbol{u})+\frac{\boldsymbol{\nabla}p}{\rho_0}=\mathbf{0} \tag{3}$$

and by extension, $\boldsymbol{\nabla}\times(\boldsymbol{\nabla}\varphi)=\mathbf{0}$, to a Bernoulli equation for the velocity potential, φ. As indicated by several authors ([9, p. 22]; [10, p. 943]) studying the simplified case of a 1D velocity through the aperture, p should be in phase with $\boldsymbol{u}\cdot\boldsymbol{u}$. The validity of this assumption follows from the observation that otherwise an oscillatory pressure would induce a fictitious bias flow through the aperture, unrelated to acoustic streaming, and consequently, a nonphysical asymmetry between in- and outflow. The statement above can be verified by expanding the solution as Fourier series and applying the harmonic balance method to determine the coefficients, where the propagation of the effect to all velocity components rests on a similar argument (cf. Appendix A). Therefore, we need to introduce the multiplicative factor $\mathbf{C}=\mathbf{diag\ sign\ u}$, ultimately resulting in

$$\frac{\partial \varphi}{\partial t}+\frac{1}{2}\boldsymbol{\nabla}\varphi\cdot\mathbf{C}\cdot\boldsymbol{\nabla}\varphi+\frac{p}{\rho_0}=\frac{p_\infty}{\rho_0}, \tag{4}$$

where p_∞ denotes the far field pressure. Analogously, recalling the form of the scalar Laplacian, $\boldsymbol{\nabla}\cdot(\boldsymbol{\nabla}\varphi)=\boldsymbol{\nabla}^2\varphi$, transforms (1) to a Laplace equation for the velocity potential

$$\boldsymbol{\nabla}^2\varphi=0. \tag{5}$$

The geometry of the problem (cf. Fig. 1) dictates vanishing normal velocity at the rigid wall separating the two half-spaces, hence, the boundary condition for (5) (in cylindrical coordinates) reads

$$\frac{\partial \varphi}{\partial z}=0 \quad \text{on} \quad r\in(R,\infty)\wedge\theta\in[-\pi,\pi]\wedge z=0. \tag{6}$$

This also permits the straightforward construction of Green's function with vanishing normal derivative at the boundary [see e.g. 29, p. 57]

$$G(\boldsymbol{x}|\tilde{\boldsymbol{x}})=\frac{1}{4\pi}\sum_{n=0}^{1}\frac{1}{\sqrt{|\boldsymbol{x}|^2+|\tilde{\boldsymbol{x}}|^2-2r\tilde{r}\cos(\theta-\tilde{\theta})-(-1)^n 2z\tilde{z}}} \tag{7}$$

and by the standard transformation and application of Green's identities

$$\varphi(\boldsymbol{x},t)=\int_\Omega \underbrace{\delta(\boldsymbol{x}-\tilde{\boldsymbol{x}})}_{=\boldsymbol{\nabla}^2 G}\varphi(\tilde{\mathbf{x}},t)\,\mathrm{d}v=\int_\Omega G\underbrace{\boldsymbol{\nabla}^2\varphi}_{=0}\,\mathrm{d}v+\oint_{\partial\Omega}\varphi\underbrace{\boldsymbol{\nabla}G\cdot\mathbf{ds}}_{=0}-\oint_{\partial\Omega}G\boldsymbol{\nabla}\varphi\cdot\mathbf{ds}, \tag{8}$$

to express the solution of (5) in each of the half-spaces, $z_\pm\in(0^\pm,\pm\infty)$, in terms of a boundary integral at $z=0$, i.e.

$$\varphi_\pm=\varphi(\boldsymbol{x}_\pm,t)=\pm\frac{1}{2\pi}\int_0^R\int_0^{2\pi}\frac{u_{z_0}(\tilde{r},\tilde{\theta},t)\tilde{r}\,\mathrm{d}\tilde{\theta}\mathrm{d}\tilde{r}}{\sqrt{r^2+\tilde{r}^2-2r\tilde{r}\cos(\theta-\tilde{\theta})+z^2}}, \tag{9}$$

where the (nonzero) boundary integral (8) is restricted to the orifice of radius R due to the boundary condition (6).

We should note that $\mathbf{ds}$ indicates the *outward* surface element vector and emphasize that a homogeneous Neumann boundary condition on G is permissible due to the infinite surface of the boundary [see 29, pp. 38–40]. Additionally, note that due to the oscillatory nature of the considered response, particle displacement takes place only in the narrow near field of the aperture as discussed by [9].

Nevertheless, the problem formulation is not yet complete, since the normal velocity inside the aperture is unknown. This missing boundary condition is determined from the Bernoulli equation (4) by the following argument. Due to irrotationality within the half space, (4) is valid in the whole domain of interest, rather than only along individual streamlines. Therefore, we can introduce a boundary condition on the pressure in the far field, $p_{\pm\infty}$, and at the aperture, $p(r,\theta,z=0^+)=p(r,\theta,z=0^-)$ [cf. 17, pp. 354–360], hence

$$\frac{\partial \varphi_+}{\partial t}+\frac{1}{2}\boldsymbol{\nabla}\varphi_+\cdot\mathbf{C}_+\cdot\boldsymbol{\nabla}\varphi_+-\frac{p_{+\infty}}{\rho_0}=\frac{\partial \varphi_-}{\partial t}+\frac{1}{2}\boldsymbol{\nabla}\varphi_-\cdot\mathbf{C}_-\cdot\boldsymbol{\nabla}\varphi_--\frac{p_{-\infty}}{\rho_0}, \tag{10}$$

which provides the relation between near and far field, and the remaining boundary condition on φ at the aperture.

Under the assumption of uniform, time-dependant forcing pressure differential in the far field away from the aperture, $p(t)=p_{+\infty}(t)-p_{-\infty}(t)$, or analogously, normally incident plane wave with large wave length compared to the size of the aperture, substitution of (9) into (10) yields the closed form problem

$$\frac{1}{\pi}\frac{\partial}{\partial t}\int_0^R\int_0^{2\pi}\frac{u_{z_0}(\tilde{r},t)\tilde{r}\,\mathrm{d}\tilde{\theta}\mathrm{d}\tilde{r}}{\sqrt{r^2+\tilde{r}^2-2r\tilde{r}\cos\tilde{\theta}}}+|u_{z_0}(r,t)|u_{z_0}(r,t)=\frac{p(t)}{\rho_0}. \tag{11}$$

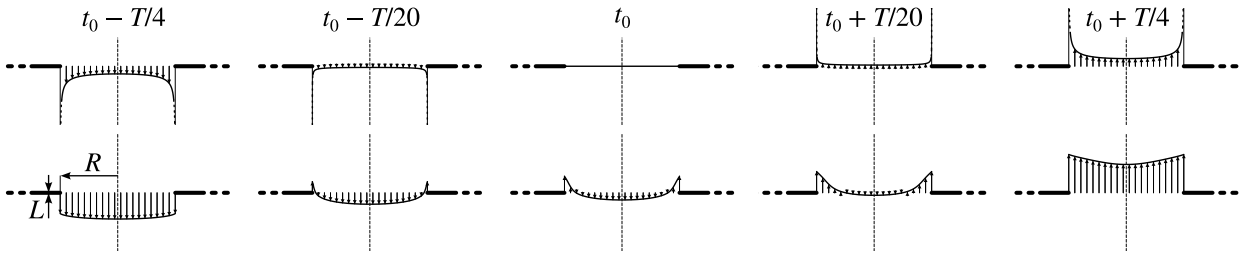

Fig. 1. Schematic representation of the normal velocity through a compact aperture in an infinite wall, subject to acoustic pressure forcing. The velocity profile is illustrated during half-cycle for the linear (top) and nonlinear problem (bottom).

2.1. Solution of the linear problem

Consider the linearized (11) [cf. 17, 354–360], which is equivalent to Weber's classical problem of the uniformly charged disc and can be formally solved, e.g. by Mellin transform [for detailed discussion see 30, pp. 334–337]. Further assuming continuity of the forcing function, the solutions for the velocity potential φ and the aperture normal velocity u_{z_0} (cf. Fig. 1; top) read

$$\varphi(r,\theta,z,t) = \varphi(t)\sin^{-1}\left(\frac{2R}{\sqrt{(R-r)^2+z^2}+\sqrt{(R+r)^2+z^2}}\right) \tag{12}$$

and

$$u_{z_0}(r,t) = \frac{\varphi_a(t)}{\pi\sqrt{R^2-r^2}}, \tag{13}$$

respectively, where $\varphi(t) = \int_0^t p(t)/\rho_0 \mathrm{d}t$. Note that in oblate spheroidal coordinates [see 29, p. 135] the potential is elementary function of only one space variable and the contravariant velocity component is constant, however, cylindrical coordinates are more convenient for the further analysis and are thus pertained for henceforth.

2.2. Numerical approximation

Since finding a closed form solution to a nonlinear integral equation like (11) is unlikely in general, it is sensible to apply the boundary element method to solve it numerically and verify the setup of the method using the exact solution for the linear case.

Due to the simplicity of the problem ($u_{z_0} \neq f(\theta)$), (11) can be transformed to a Fredholm integral equation by analytically integrating w.r.t. θ in the first term, therefore, even collocation with piecewise constant elements converges [31]. Nevertheless, the accuracy (and convergence) of the method still relies on the evaluation of element integrals, therefore, this is done analytically here.

The inner integral in (11) can be transformed into algebraic form by performing few algebraic operations [see 32, Lemma 1]

$$\int_0^{2\pi} \frac{u_{z_0}(\tilde{r},t)\tilde{r}\ \mathrm{d}\tilde{\theta}}{\sqrt{r^2+\tilde{r}^2-2r\tilde{r}\cos\tilde{\theta}}} = 4\int_0^{\mathrm{Min}(r,\tilde{r})} \frac{u_{z_0}(\tilde{r},t)\tilde{r}\ \mathrm{d}\tau}{\sqrt{r^2-\tau^2}\sqrt{\tilde{r}^2-\tau^2}}. \tag{14}$$

Since the velocity field is discretized into elements, for any value of r, the integral in (11) is represented as a linear combination of the individual element integrals, $I = \sum_{i=1}^{N} u_{z_0 i} I_i$. Those can be separated into three groups, depending on the position of r relative to the element: r is inside, in front or behind the element. In the first case the element integral reads

$$I_i = 4\left[\int_{R_{i-}}^{r}\int_0^{\tilde{r}} \frac{\tilde{r}\ \mathrm{d}\tau\mathrm{d}\tilde{r}}{\sqrt{r^2-\tau^2}\sqrt{\tilde{r}^2-\tau^2}} + \int_r^{R_{i+}}\int_0^{r} \frac{\tilde{r}\ \mathrm{d}\tau\mathrm{d}\tilde{r}}{\sqrt{r^2-\tau^2}\sqrt{\tilde{r}^2-\tau^2}}\right], \tag{15}$$

which after inverting the integration order results in

$$I_i = 4\left[\int_0^{R_{i-}} \frac{1}{\sqrt{r^2-\tau^2}}\int_{R_i^-}^{R_{i+}} \frac{\tilde{r}\ \mathrm{d}\tilde{r}}{\sqrt{\tilde{r}^2-\tau^2}}\mathrm{d}\tau + \int_{R_{i-}}^{r} \frac{1}{\sqrt{r^2-\tau^2}}\int_\tau^{R_{i+}} \frac{\tilde{r}\ \mathrm{d}\tilde{r}}{\sqrt{\tilde{r}^2-\tau^2}}\mathrm{d}\tau\right] \tag{16}$$

and thus,

$$I_i = 4\left[R_{i+}\mathrm{E}\left(\frac{r^2}{R_{i+}^2}\right) - r\mathrm{E}\left(\frac{R_{i-}^2}{r^2}\right) - \frac{R_{i-}^2-r^2}{r}\mathrm{K}\left(\frac{R_{i-}^2}{r^2}\right)\right], \tag{17}$$

where K and E denote the complete elliptic integral of the first and second kind, respectively. Analogously, one can evaluate the element integrals in case of r being in front

$$I_{i-} = \int_{R_{i-}}^{R_{i+}}\int_0^{2\pi} \frac{\tilde{r}\ \mathrm{d}\tilde{\theta}\mathrm{d}\tilde{r}}{\sqrt{r^2+\tilde{r}^2-2r\tilde{r}\cos\tilde{\theta}}} = 4\left[R_{i+}\mathrm{E}\left(\frac{r^2}{R_{i+}^2}\right) - R_{i-}\mathrm{E}\left(\frac{r^2}{R_{i-}^2}\right)\right] \tag{18}$$

and behind the element

$$I_{i+} = 4\left[r\mathrm{E}\left(\frac{R_{i+}^2}{r^2}\right) + \frac{R_{i+}^2 - r^2}{r}\mathrm{K}\left(\frac{R_{i+}^2}{r^2}\right) - r\mathrm{E}\left(\frac{R_{i-}^2}{r^2}\right) - \frac{R_{i-}^2 - r^2}{r}\mathrm{K}\left(\frac{R_{i-}^2}{r^2}\right)\right]. \tag{19}$$

Note that from here it is simple to obtain both collocation and Galerkin formulation, by choosing any $R_{j^-} < r_j < R_{j^+}$ for each element in the former, or integrating w.r.t. r from R_{j^-} to R_{j^+} in the latter case. Furthermore, similar expressions can be obtained for any even order spline elements, however, the gains in accuracy are found to be insignificant for the used mesh and a collocation method is chosen for simplicity.

For the following calculations the aperture is discretized with fifty elements. The collocation points are chosen in the middle of each element, where the mesh density is increasing towards the edge of the aperture, proportional to the expected gradient (cf. Fig. 1).

2.3. Effects of finite wall thickness

The previously discussed model assumes infinitely thin aperture, therefore, it needs to be extended if finite thickness, $L \neq 0$, is to be considered. The most reliable approach would be to consider finite space with appropriate geometry representing the aperture and to construct a Green's function satisfying the corresponding boundary conditions [see e.g. 33–35]. Furthermore, for thick walls one should also account for the vorticity shed by the leading edge of the aperture and convected inside it [36, p. 6]. On the other hand, the assumption that streamlines inside the aperture run orthogonal to its cross section seems to yield good results for thin, i.e. $L \ll D$, apertures [see e.g. 17, Chapter 5]. Additionally, constructing Green's functions for confined spaces would require infinite series expansion, even for the simplest geometries. Since this study is focused on the thin wall problem, rather than the effects of wall thickness, and the main reason for considering it at all is comparison to experiments conducted on (technically) sharp edged orifices, we adopt Howe's approach for simplicity. This leads to a modified pressure boundary condition at the aperture, namely, the emergence of inertia term, $p(r,\theta,z=0^+) = p(r,\theta,z=0^-) - \rho_0 L\partial u_{z_0}/\partial t$ [cf. 17, pp. 354–360], which ultimately results in an aperture equation of the form

$$\frac{\partial}{\partial t}\left(\frac{1}{\pi}\int_0^R\int_0^{2\pi}\frac{u_{z_0}(\tilde{r},t)\tilde{r}\,\mathrm{d}\tilde{\theta}\mathrm{d}\tilde{r}}{\sqrt{r^2+\tilde{r}^2-2r\tilde{r}\cos\tilde{\theta}}} + Lu_{z_0}(r,t)\right) + |u_{z_0}(r,t)|u_{z_0}(r,t) = \frac{p(t)}{\rho_0}. \tag{20}$$

3. Results

In this section the predictions of the previously described model are compared to experimental results from the literature and direct numerical simulations performed for the occasion. Section 3.1 focuses on the experimental velocity data of [7], obtained by means of hot wire anemometer placed at the center of the aperture. The comprehensiveness of the study allows for detailed comparison of amplitude, phase and time trace of the absolute velocity at the center of the aperture. Conversely, Section 3.2 is concerned with the experiments of [10], where the reported data on the transmitted pressure, resulting from complex forcing patterns, permits a detailed investigation of both transient behavior and steady state spectrum of the average aperture velocity. Subsequently, in Section 3.3, a direct numerical simulation of the problem is used as a basis for investigating the spatial–temporal behavior of the reduced order representation in further detail. Consequently, Section 3.4 applies the already validated model to predict influence of various parameters on the nonlinear aperture dynamics.

3.1. Ingard & Ising's experiment

In the following we compare our model predictions and the experimental measurements from [7] [cf. Fig. 2(a)–(b)], where to also study the effects of the aperture diameter on the model, we discuss results for $D \in [7\text{ mm}; 9\text{ mm}]$. The sold lines indicate predictions for $D = 8.5$ mm and the shaded regions illustrate the results for $D \in [7\text{ mm}; 9\text{ mm}]$, where, naturally, the edges closest to the black lines correspond to $D = 9$ mm.

It is worth mentioning that for most aperture diameters in the range [8.5 mm; 9 mm] [cf. Fig. 2(a)], model predictions fall within the $\pm 3\%$ accuracy of the velocity measurements reported in [7, table I]. Also note that even the distinguishable deviations at $D = 7$ mm (the reported orifice diameter) and $D = 9$ mm are small in absolute value (<0.5 m/s), which is somewhat obscured by the logarithmic scale of the plot. Additionally, we need to emphasize that both amplitude and phase difference refer to the absolute velocity at the center of the aperture as directly measured by the accordingly placed hot wire anemometer, whose wire length is small compared to the orifice diameter.

A general trend of the model warranting a detailed discussion is the velocity dependence on the forcing pressure and aperture diameter. At small forcing amplitudes (and essentially linear response), pressure and velocity are approximately proportional in amplitude and out of phase ($X \approx \text{const.}$; $R \ll 1$), while in the strongly nonlinear regime the pressure amplitude is proportional to the squared velocity amplitude [cf. Fig. 2(a)] and the phase difference is decreasing [cf. Fig. 2(b)], which is consistent with experiments over wide variety of conditions (see e.g. [12] for a survey). Furthermore, the aperture velocity is inversely proportional to the diameter in the nearly linear range and practically independent of it at high amplitudes. Inspecting (20) reveals that the only term depending on the aperture dimensions is the rate of change of the specific inertia, hence, at high velocities the system response is nearly independent of equivalent mass, indicating quasi-steady behavior consistent with the experimental observations

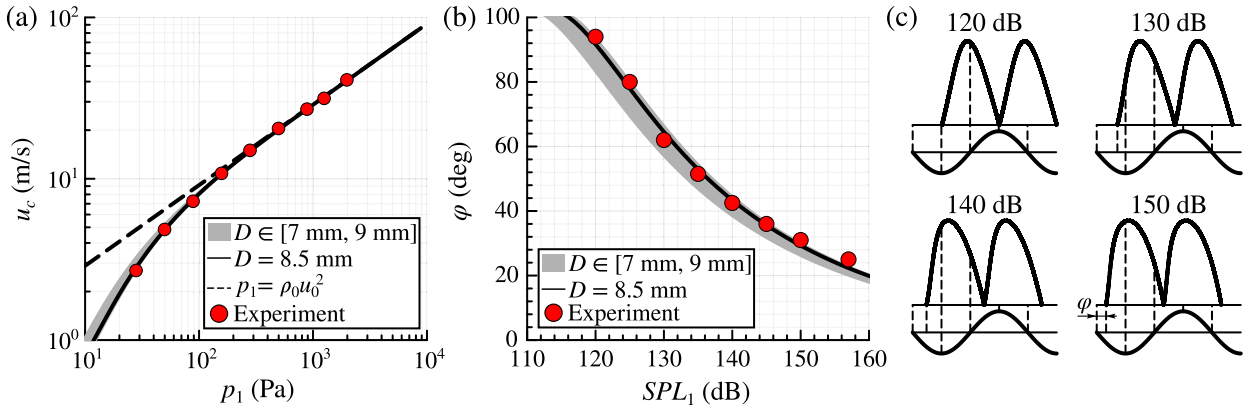

Fig. 2. Comparison between the model predictions and the experimental measurements of [7] for (a) forcing pressure amplitude vs. velocity amplitude at the center of the aperture, (b) forcing SPL vs. phase lag of the velocity w.r.t. the forcing pressure and (c) time traces at different SPL. The reference pressure of all dB scales is 28×10^{-6} Pa.

of [8] and [9, p. 34]. Fig. 2(a) illustrates the latter statement, since changes of the aperture diameter, and by extension — mass inertia, are shown to be important at low velocity amplitudes and to have little to no influence at large ones.

This further lends credibility to the [10, sec. V] hypothesis that the details of the vorticity generation can be drastically simplified while still accurately capturing the relevant global quantities like the mass flow through the aperture or the velocity profile at the in-flow plane. In particular, the predominantly quasi-static nature of the aperture at large forcing amplitudes, which is well reproduced by Eq. (11), would be unlikely to occur if the rather dynamic nature of the detailed vortex motions [cf. 23, fig. 4 or fig. 4 below] are dominating the mass flow. Furthermore, based on dimensional analysis, [9, p. 34] concludes that (i) reactance, which is conjugate quantity to the apparent mass of the fluid near the aperture and therefore related to the inertia term, is only dominant at the beginning of the cycle when the amplitudes are small, and (ii) irrotationality in the two half spaces and a tangential velocity jump at the aperture are reasonable assumptions. For larger amplitudes the behavior of the system seems to be governed by a quasi-static resistance term. Our model is consistent with these findings, as evident by inspection of Eq. (11), where the inertia term can be seen to control the balance of momentum at low velocities u_{z_0} and to increasingly loose importance to the static resistance term, $u_{z_0}|u_{z_0}|$, as amplitudes grow. In this case, the resistance and the corresponding modulation of velocity amplitude, profile and phase shift are inherently nonlinear effects and the related linear representation yields unusable results at high forcing pressures, e.g. $\bar{u}_c > 200$ m/s at $p_1 = 2000$ Pa and even higher near the edges.

Another important feature of the nonlinear aperture flow is the distortion of the input signal due to excitation of higher harmonics as discussed by several authors [e.g. 6,7,11]. Fig. 2(c) shows the time traces of the velocity predicted by the model for harmonic forcing at different sound pressure levels (SPLs), where the plotting format of the oscilloscope traces reported in [7, Fig. 2] has been adopted for comparison reasons. Close inspection of Fig. 2(c) and its counterpart in the aforementioned reference shows that the general shape of the time trace corresponding to predicted and measured velocity is virtually identical, while Fig. 2(a)–(b) shows that the same holds also for the amplitude and phase. Again, the linear representation is not equipped for reproducing such effects and would not experience any velocity trace distortion.

It is also important to emphasize that all of the velocity measurements reported in [7] were obtained by means of a hot wire anemometer placed at the center of the aperture, and therefore, correspond to $u_{z_0}(0,0,t) = u_c(t)$. This is relevant for the discussed results at all amplitudes, since in the quasi-linear regime the velocity profile is non-uniform, while at high amplitudes the phase difference between velocities at different positions within the aperture becomes significant (cf. Fig. 1).

3.2. Cummings' experiment

The experiments of [10] consider more realistic forcing functions, leading to waves with complex shape impinging on the aperture, and therefore, are suitable for studying the transient behavior of the model. Additionally, due to its vary high forcing amplitude and emerging periodicity, the last example [10, Fig. 15] is also appropriate for investigating the fidelity of the predicted spectrum in the steady state. Finally, the reported measurements refer to the transmitted pressure, hence, are pertinent for validating the predictions of the average velocity trough the aperture, in contrast with the point-like nature of the hot wire data discussed in Section 3.1.

The setup of the aforementioned experiment includes a sharp-edged orifice of $R = 1.65$ mm located in an impedance tube with $D_{\mathrm{IT}} = 50$ mm, where the periodic forcing pressure, $p_1(t)$, of frequency $f = 643$ Hz is measured shortly before and the transmitted pressure, $p_2(t)$, shortly after the aperture.

Since the aperture is only described as "sharp-edged", for the following calculations we set $L = 0$. Additionally, on account of the relative proximity of the measurement point, signal distortions due to nonlinear wave propagation effects are expected to be negligible. Therefore, we assume linear acoustics after the aperture and consequently, the latter is treated as a plane acoustic source

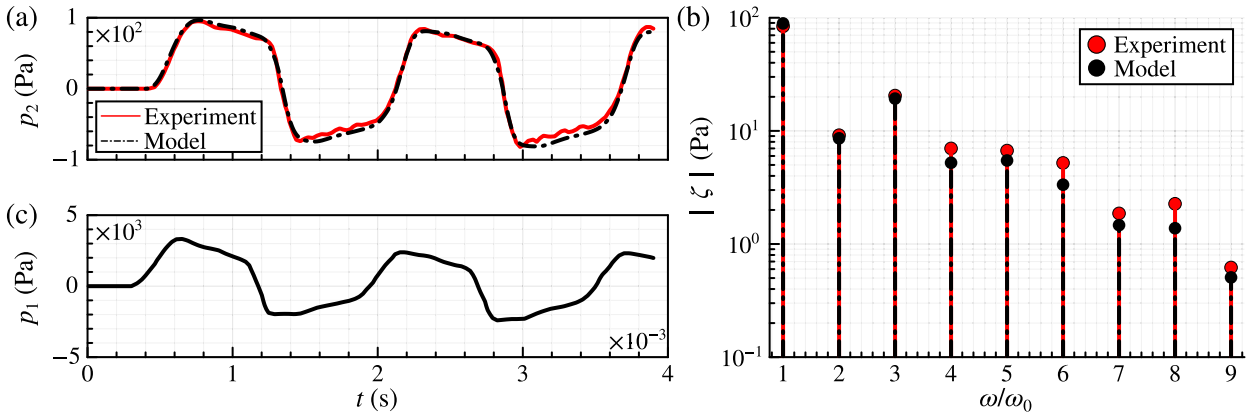

Fig. 3. Comparison between the model predictions and the experimental measurements of [10] for (a) the time trace and (b) the spectrum, of the transmitted pressure, $p_2(t)$, resulting from (c) the forcing pressure, $p_1(t)$.

radiating into a tube. Hence, the transmitted pressure in the far field, $p_2(t)$, can be calculated in terms of the impedance of air, ρc, the average velocity in the aperture, $U(t)$, and its area ratio with the tube, σ, as

$$p_2(t) = \frac{\rho_0 c}{A_{TT}} \int_0^R \int_0^{2\pi} \tilde{r} u_{z_0}(\tilde{r}, t)\, \mathrm{d}\tilde{\theta}\mathrm{d}\tilde{r} = \sigma \rho_0 c U(t). \tag{21}$$

Fig. 3 shows a comparison between the model developed in Section 2 and measurements reported in [10, Fig. 15], where the response is analyzed in terms of the time series data presented in Fig. 3(a) and the spectrum shown in 3(b). The forcing, $p_1(t)$, and response, $p_2(t)$, functions are reproduced from figure 15 of the aforementioned reference using 120 and 170 points, respectively, while all intermediate values are determined by linear interpolation as needed.

The forcing pressure, $p_1(t)$, recorded in Fig. 3(c) starts from a standstill, exciting the transient response we want to study, and after experiencing some transient behavior of its own in the first cycle, settles to a steady state. The transmitted pressure, $p_2(t)$, follows a similar pattern, where, by inspecting Fig. 3(a) we can conclude that the model predicts this transient response well. Analogously to $p_1(t)$, the transmitted pressure, $p_2(t)$, reaches a steady state after the first cycle as observed in [10], therefore, we can calculate the Fourier series expansion of the corresponding periodic signal, resulting in a discrete spectrum with fundamental frequency of $f = 643$ Hz. A comparison of the absolute value of the Fourier coefficients between predicted and measured response is shown in Fig. 3(b). By examining the spectrum, we can conclude that the predicted amplitudes of the fundamental frequency component and the first eight harmonics are in good agreement with the experimental data. This, in conjunction with the good prediction of the transient response, suggests that the model presented in Section 2 is also an accurate description of the "average" aperture dynamics. Comparison with other experiments reported in [10] can be found in Appendix B.

3.3. Comparison with DNS

The previous two sections assessed the ability of Eqs. (11) and (20) to predict the center and average velocity through a compact aperture by comparison to experimental measurements. To further validate the model presented in Section 2, we now turn our attention to the complete spatial–temporal evolution of the velocity profile at the in-flow plane of the orifice. Since there are no experimental studies, directly measuring the relevant quantity, we numerically approximate the problem of $D = 7$ mm aperture in $L = 0.1$ mm (quasi) infinite wall via a direct numerical simulation, utilizing the compressible solver AVBP. Since a simulation allows for unique flexibility in exploring the influence of various parameters, we utilize this fact by studying two different fluids – pure air and a modified version thereof, where the viscosity is increased 100 times.

The simulated domain is two dimensional (340 mm × 170 mm), the mesh consists of approximately 640 000 conformal quadrilateral elements, with significant density increase near the aperture (cf. inset in Fig. 4). Approximately half of the elements are concentrated within two diameters distance from the aperture. The temperature is 300 K and the two simulated fluids are, as mentioned, (1) pure air and (2) air with 100 times higher viscosity. The boundary conditions are as follows: bottom — characteristic inlet with relaxation towards reference pressure, $p_{ref} = 101\,325$ Pa, and superimposed isentropic sinusoidal acoustic pressure forcing, $p_f(t) = \bar{p}_f \sin \omega t$, with $\bar{p}_f = 160$ Pa and $f = 150$ Hz; top — free stream outlet; right — symmetry corresponding to the aperture axis; left — slip adiabatic walls; middle - no-slip adiabatic walls forming the separator wall and the aperture.

We start the analysis of the DNS by examining the vorticity shown in Fig. 4. In particular, for the pure air [cf. Fig. 4(a)–(e)] the results are consistent with the thin vortex sheet assumption of [11,23], where the vortex motions are also qualitatively similar to the discrete vortex simulation of the former [cf. 23, fig. 4]. Furthermore, a good agreement with the flow visualizations of [19, fig. 13(a)] can also be observed by comparison to Fig. 4, while inspection of Fig. 5(e) [red line] also shows that the velocity amplitude is consistent with the measurements in [7, table I]. Interestingly, from Figs. 4(f)–(j) and 5(j), we can conclude that even in the highly

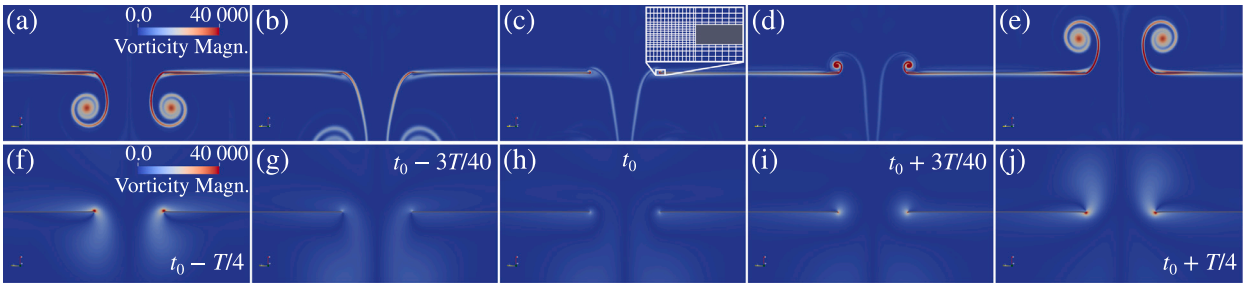

Fig. 4. Vorticity derived from DNS of a $D = 7$ mm aperture in (quasi) infinite wall forced by an acoustic pressure amplitude of $\bar{p}_i = 160$ Pa and frequency of $f = 150$ Hz. Sub-panels (a)–(e) illustrate the vorticity for different time instances throughout one acoustic forcing cycle, where the medium is pure air. Sub-panels (f)–(j) again show the vorticity throughout one acoustic forcing cycle, however, the medium has 100 times the viscosity of air. The inset shows the mesh details around the aperture edge.

viscous case, where the details of vortex shedding are vastly different, the velocity profile and amplitude remain quite similar. This observation is also consistent with the comparison [12] of numerous experimental studies conducted with air, water and oil as a working medium.

Indeed, by further investigating Fig. 5 we can deduce that the velocity profiles obtained from the DNS (red lines) and the reduced order model (ROM) of Section 2 (black dash-dot lines) exhibit reasonable degree of similarity, regardless of the two orders of magnitude higher viscosity in sub-panels 5(f)–(j). To also study the temporal behavior of both systems, a time - t_0 - is chosen, such that the average instantaneous velocity through the aperture is approximately zero and then different phase shifts are applied, analogous to Fig. 1. The aforementioned velocity profiles agree reasonably well (for both viscosity values) throughout the acoustic forcing cycle, both in terms of general trends and specific values. Additionally, the phase shift between the total center velocity and the forcing pressure, $\varphi \approx 0.001\ \text{s} \times 150\ \text{Hz} \times 360\ \text{Deg} = 54\ \text{Deg}$, also agrees well with the experiment in [7, fig. 6]. Of course, discrepancies exist between the velocity profiles resulting from the DNS and from the proposed ROM, yet the differences in the global quantities of interest, like the oscillating mass flow, are relatively small as can be deduced from the insets in Fig. 5(e) and (j). This is an important observation, since the model in Section 2 completely ignores the details of the vortex shedding and only assumes a velocity jump across the aperture and irrotationality within the half spaces.

Another important piece of information we can extract from the DNS is the pressure distribution, which, as seen in Fig. 6, is rather uniform apart from the localized low pressure zones induced by the discrete vortices. The aforementioned statement is especially fitting for the high viscosity case. This further justifies another key assumption of the reduced order model in Section 2, namely, that the nonlinearity makes substantial contribution only in the hydrodynamic near field of the aperture, extending to 2–3 diameters in each direction.

In a certain sense, Eq. (11) is the "least nonlinear" representation of the aperture flow, since the acoustic effects are assumed to be decoupled from the hydrodynamically nonlinear orifice. To solve the velocity profile problem, the incident wave is considered as an external forcing and to solve the sound propagation problem, the aperture is considered as a plane radiator with already calculated velocity profile. This approach is successfully applied for the Cummings' experiment in Section 3.2, and the DNS further confirms the acoustic compactness in the nonlinear regime also for the setup in [7].

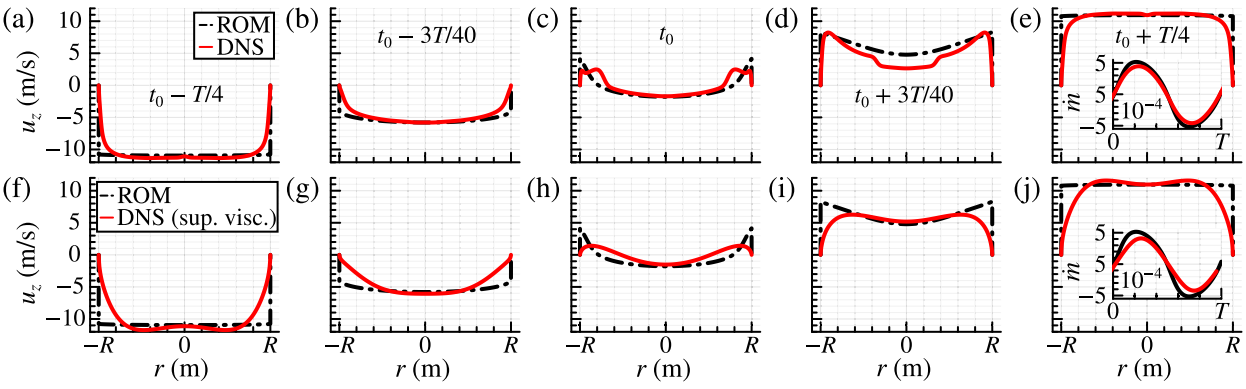

Fig. 5. Velocity at the in-flow plane of a $D = 7$ mm aperture in (quasi) infinite wall forced by an acoustic pressure amplitude of $\bar{p}_i = 160$ Pa and frequency of $f = 150$ Hz. Sub-panels (a)–(e) compare the velocity profile derived from DNS of pure air (red solid lines) and the reduced order model (ROM) of Section 2 (black dash-dot lines) for different time instances throughout one acoustic forcing cycle, where the inset in sub-panel (e) compares the mass flow $\left(\int \rho u_z \mathrm{d}s\right)$ predictions. Analogously to Fig. 4, the DNS results shown in sub-panels (f)–(j) derive from a medium with 100 times the viscosity of air, where once more, the sub-panels illustrate the velocity profile derived from DNS (red solid lines) and ROM (black dash-dot lines), and the inset in (j) compares the mass flows.

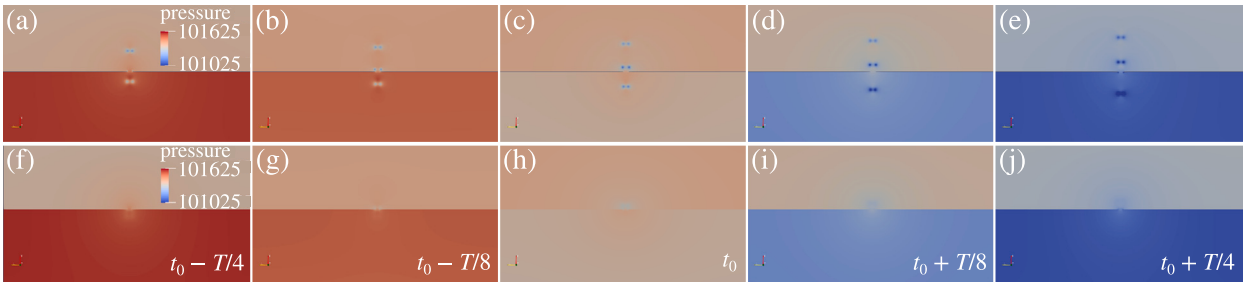

Fig. 6. Pressure distribution resulting from a sinusoidal acoustic pressure wave of amplitude $\bar{p}_f = 160$ Pa and frequency $f = 150$ Hz incident on a $D = 7$ mm aperture in (quasi) infinite wall. Sub-panels (a)–(e) illustrate the pressure for five equidistant time instances throughout one acoustic forcing cycle, where the medium is again pure air. Conversely, sub-panels (f)–(j) once more show results (pressure) for a medium with 100 times the viscosity of air.

3.4. Model predictions

After validating the model proposed in Section 2 against the experimental data of [7,10], as well as against the direct numerical simulation of the previous section, here we use it to address some unexplored aspects of the system behavior. In particular, [7, fig. 7; fig. 14] use two different experimental techniques to determine the orifice impedance under free space termination ($X \approx 10$ kg/m^{2}s vs. $X \approx 8$ kg/m^{2}s) and attribute the mismatch between them to large experimental error (≈20%) of the hot wire measurements at low velocity amplitudes (≈3–5 m/s). Although such scenario cannot be completely ruled out, a more likely explanation is that while the impedance in fig. 7 relates the forcing pressure to the fundamental component of the velocity at the *center* of the aperture, the resonator measurements in fig. 14 are function of the *average* aperture velocity. Fig. 7(a) illustrates the discrepancy between the two impedance definitions (top), caused by the non-uniformity of the velocity profile at low amplitudes (bottom), which is also consistent with the experimentally observed differences (red line vs. red markers). As expected from the previously discussed results, the differences decrease with increasing velocity amplitude, since the velocity gradients in radial direction are becoming less prominent, i.e. the profile flattens. In [7, Fig. 20] a (weighted) superposition of the two measurement techniques is adopted to determine the (collective) impedance over the whole range of velocities, and as illustrated in Fig. 7(a), the *average* velocity based impedance of the model fits this data reasonably well, where the setup is identical to Section 3.1. Furthermore, the *center* velocity based impedance of the model fits the hot wire technique [7, fig. 7] reasonably as well, suggesting validity of the hypothesized cause of the discrepancy. Another unexplored topic of interest is the collective dependence of the average velocity on the forcing frequency and pressure amplitude (cf. Fig. 7(b) and (c), respectively). An inspection of the former confirms the [7] conjecture that at high forcing SPL, where resistance dominates, the aperture velocity is nearly independent of frequency. This is also the operating stage where *average* and *center* velocity are practically identical. Furthermore, by studying Fig. 7(c) we can conclude that the forcing pressure amplitude at which the system starts exhibiting nonlinear behavior is frequency dependent. For example, at $f = 10$ Hz all considered forcing SPLs (110 dB−170 dB) lead to a strongly nonlinear behavior, while at $f = 1$ kHz even a forcing of 170 dB barely enters the quasi-steady regime.

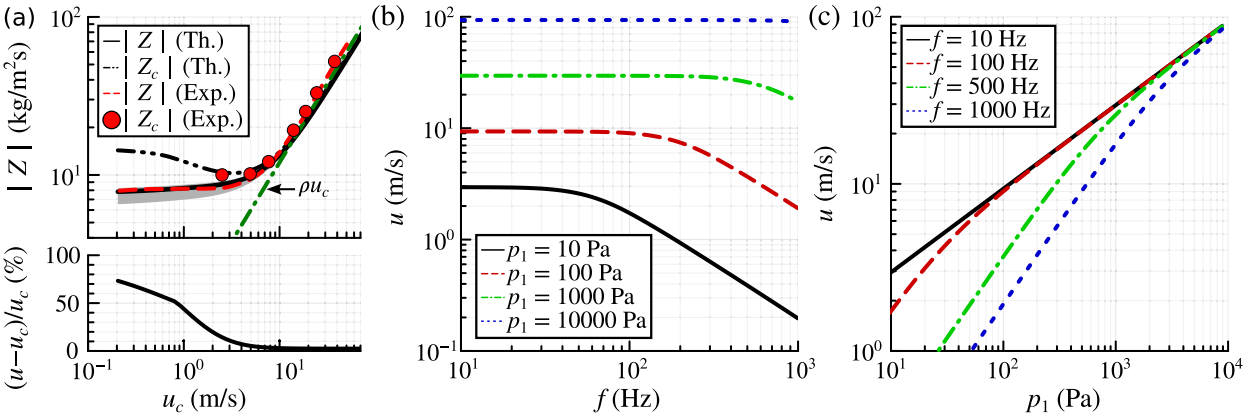

Fig. 7. The proposed model is used (a) to explain differences in the impedance based on the average and center velocity (top), depending on their relation (bottom). The top sub-panel shows comparison with the average velocity based impedance data of [7, Fig. 20] (red dashed line) and the center velocity based impedance data of [7, Fig. 7] (red circular markers), where the setup is identical to Section 3.1, since the same dataset is analyzed. The model is also applied to predict the average velocity dependence on (b) forcing frequency and (c) pressure amplitude.

4. Conclusion

The present work introduces a mathematical model describing the dynamics of an acoustically compact aperture under arbitrary pressure forcing, successfully validates it against well established experimental results and direct numerical simulations performed for the occasion, and applies it to resolve some issues of interest.

The fluid mechanical model developed in Section 2 is derived from the fundamentals of classical mechanics, albeit under significant simplifications. This offers advantages in the intuitive understanding of the dominant physics of the problem and facilitates the modeling of more sophisticated systems by allowing the flexibility of working directly with the continuum representation or simplifying it to a lumped parameter model via nonlinear reduction techniques.

Furthermore, a comparison with established experimental data from the literature shows good agreement in both general trends and specific values. In Section 3.1, a detailed collation of model predictions and the hot wire data of [7] exemplifies the good agreement in amplitude, phase and time trace of the velocity at the center of the aperture. In Section 3.2 the transmitted pressure measurements of [10] confirm the accuracy of the average velocity's time response and spectrum. Additionally, Section 3.3 explores the spatial–temporal characteristics of the approximation in greater detail by utilizing a DNS of the problem as reference solution.

Based thereon, in Section 3.4 the model is used to explain experimentally observed discrepancies between different impedance measurement techniques and to explore the frequency dependence of the aperture dynamics at different forcing pressure amplitudes.

A natural application of this simplified aperture representation would be the modeling of the practically relevant case of a perforated liner. In first approximation, it might be sufficient to consider contributions with decreasing magnitude to the integral in Eq. (9). In particular, the latter is defined over the whole infinite plane and for a perforated liner there will be multiple sections with nonzero normal velocity and they will all contribute to the inertia term accordingly. Nevertheless, the question of when the discrete apertures start to influence each other significantly needs to be carefully addressed before proposing and validating such model, and this is beyond the scope of this study.

Finally, we should comment on the limitations of the model proposed in Section 2. In particular, the reduced aperture representation we propose rests on significant simplifications of the flow near field, specifically targeting acoustics applications. Clearly, if specific flow features, e.g. vortex generation, are of interest the model is not providing any useful information. As with any reduced order modeling task, we only consider the dominant mechanism responsible for explaining the effects we are interested in, i.e., the nonlinear impedance and acoustic transmission of a compact orifice. Consequently, linear reactance effects are considered, however, linear resistance is not, i.e., the latter contains only (relevant) nonlinear terms. For strongly differing use, e.g. acoustic non-compactness or presence of non-negligible streaming effects, the model is not expected to perform well. Given the reduction of all vorticity effects to a velocity jump at the aperture plane, the model should be used with caution for cases not discussed herein.

CRediT authorship contribution statement

Alexander K. Stoychev: Formal analysis, Investigation, Methodology, Validation, Writing – original draft, Writing – review and editing. **Nicolas Noiray:** Conceptualization, Investigation, Writing – review and editing, Supervision.

Declaration of competing interest

The authors declare that they have no known competing financial interests or personal relationships that could have appeared to influence the work reported in this paper.

Data availability

No data was used for the research described in the article.

Appendix A. Nonlinear resistance

In the following we outline the argument for the specific form of the resistance term of Eq. (4) in greater detail. Starting from the one dimensional special case of Eq. (3) we have

$$\frac{\partial u}{\partial t} + \frac{1}{2}\frac{\partial}{\partial z}(u^2) + \frac{1}{\rho_0}\frac{\partial p}{\partial z} = 0, \tag{A.1}$$

which simplifies to

$$\frac{\partial \varphi}{\partial t} + \frac{1}{2}\left(\frac{\partial \varphi}{\partial z}\right)^2 + \frac{p}{\rho_0} = \frac{p_\infty}{\rho_0} \tag{A.2}$$

and ultimately leads to the aperture equation

$$\frac{\partial \varphi}{\partial t} + \frac{1}{2}\left(\frac{\partial \varphi}{\partial z}\right)^2 = \frac{p_{\bar{\Gamma}}}{\rho_0}, \tag{A.3}$$

with $p_f(z,t) = \bar{p}_f \sin(kz - \omega t)$ being the forcing pressure, i.e., the incident wave. Introducing the standard ansatz

$$\varphi(z,t) = \Psi_0(z) + \sum_{n=1}^{N} \left[\Phi_n(z) \sin n\omega t + \Psi_n(z) \cos n\omega t\right] \tag{A.4}$$

yields the following for the time independent component

$$\Psi_{0,z}(z) + \frac{1}{2} \sum_{n=1}^{N} \left[\Phi_{n,z}(z) + \Psi_{n,z}(z)\right] = 0, \tag{A.5}$$

where $(\cdot)_{,z} \equiv \partial(\cdot)/\partial z$ indicates the spatial derivative. The expressions for the fundamental frequency and its harmonics are more involved, yet their exact form is not essential for the discussion. Solving the resulting equations is clearly a difficult task, however, the key point here is that as long as the summation term does not yield zero, there will also be nonzero $\Psi_{0,z}(z)$, which corresponds to a constant flow velocity through the aperture due to $u_z = \partial\varphi/\partial z$. In the simplest case of $N = 1$ the expressions for the fundamental component are concise

$$\omega\Psi_1(z) - \Psi_0(z)\Phi_1(z) = \bar{p}_f \cos(kz) \tag{A.6}$$

$$\omega\Phi_1(z) + \Psi_0(z)\Psi_1(z) = \bar{p}_f \sin(kz), \tag{A.7}$$

hence, it is easy to verify that $\Psi_{0,z}(z) \neq 0$. Furthermore, from the size of the constant term one can deduce that the observed effect cannot be related to acoustic streaming. Analogous conclusion can also be reached when higher harmonics are considered. The effect discussed above is directly related to the fact that $f(z) = z^2$ is an even function, hence, the solution to the integro-differential equation will essentially inherit this behavior and any Fourier series expansion thereof will contain constant terms. The natural approach to the issue would be transforming the problematic term in an odd function, i.e. $f(z) = |z|z$, as done by e.g. [10, p. 943].

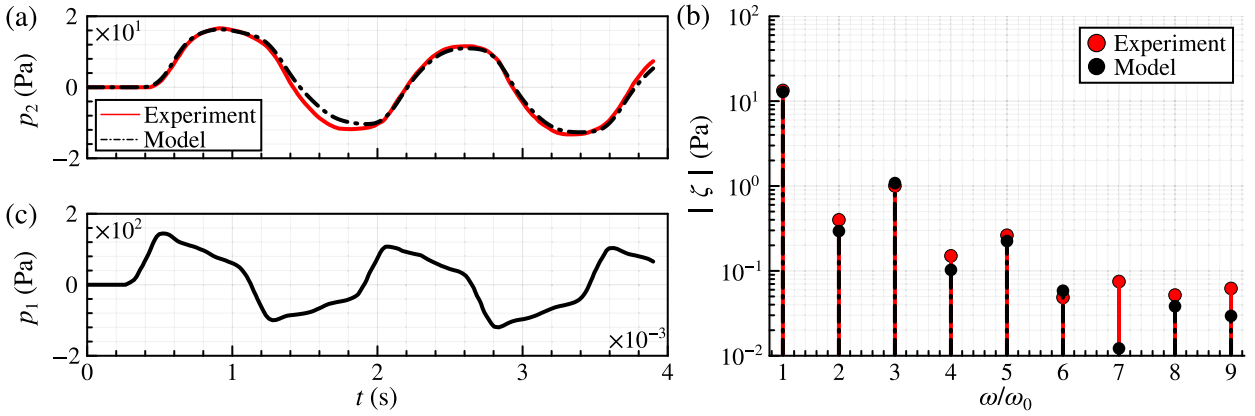

Fig. 8. Comparison between the model predictions and the experimental measurements of [10] for (a) the time trace and (b) the spectrum, of the transmitted pressure, $p_2(t)$, resulting from (c) the forcing pressure, $p_1(t)$. This case considers the low amplitude periodic excitation.

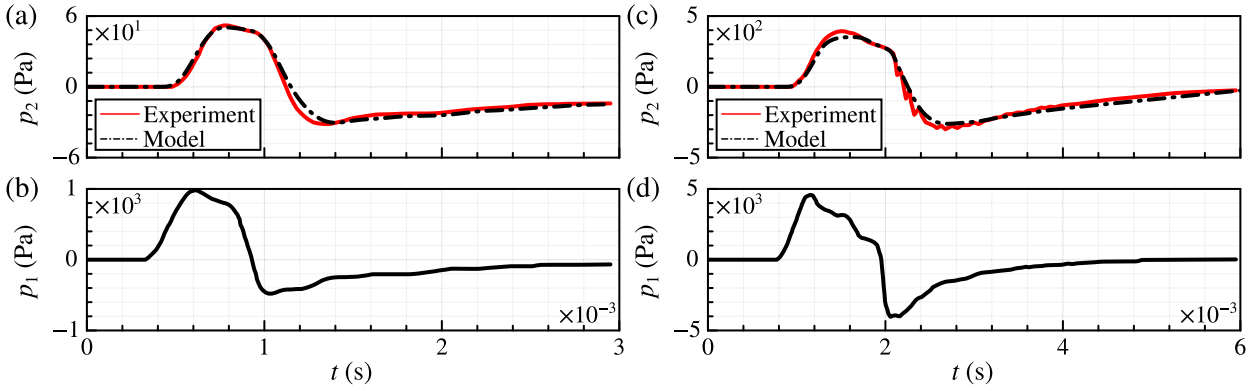

Fig. 9. Comparison between the model predictions and the experimental measurements of [10] for (a) the transmitted pressure, $p_2(t)$, through a sharp edged aperture, resulting from (b) the non-periodic forcing pressure, $p_1(t)$. Additionally, the agreement between predicted and measured (c) transmitted pressure, $p_2(t)$, through a thick aperture, resulting from (d) the non-periodic forcing pressure, $p_1(t)$, is also shown to be good. Nevertheless, this is not expected in general, since the effects of aperture thickness are only roughly estimated in the proposed model.

In the three dimensional case the considerations above should be valid in any direction, since it is always possible to assume one dimensional wave incident at an arbitrary angle w.r.t. the aperture and then to subsequently apply the presented reasoning. Therefore, we need to propagate the aforementioned transformation to all velocity components, resulting in

$$\frac{\partial \varphi}{\partial t} + \frac{1}{2}\left[\left|\frac{\partial \varphi}{\partial x}\right|\frac{\partial \varphi}{\partial x} + \left|\frac{\partial \varphi}{\partial y}\right|\frac{\partial \varphi}{\partial y} + \left|\frac{\partial \varphi}{\partial z}\right|\frac{\partial \varphi}{\partial z}\right] = \frac{p_f}{\rho_0}. \tag{A.8}$$

Appendix B. Further validation of the transmission behavior

This appendix presents further comparison with the transmitted pressure experiments from [10]. In particular, Fig. 8 examines the aperture dynamics at low-amplitude periodic forcing, while Fig. 9 compares the results for non-periodic forcing. In this particular case good predictions can be observed also for a thick aperture [cf. Fig. 9(c)–(d)], however, this will not be the case generally, since the thickness effects are only roughly estimated. For a better treatment of finite thickness apertures we refer to e.g. [33–35].

References

[1] Rayleigh, The Theory of Sound, Cambridge Library Collection - Physical Sciences, vol. 2, Cambridge University Press, Cambridge, UK, 1877, http://dx.doi.org/10.1017/CBO9781139058094.
[2] Rayleigh, On the theory of resonance, Philos. Trans. R. Soc. 161 (1) (1871) 77–118, http://dx.doi.org/10.1098/rstl.1871.0006.
[3] L.J. Sivian, Acoustic impedance of small orifices, J. Acoust. Soc. Am. 7 (2) (1935) 94–101, http://dx.doi.org/10.1121/1.1915795.
[4] U. Ingard, On the theory and design of acoustic resonators, J. Acoust. Soc. Am. 25 (6) (1953) 1037–1061, http://dx.doi.org/10.1121/1.1907235.
[5] D.A. Bies, O.B. Wilson, Acoustic impedance of a Helmholtz resonator at very high amplitude, J. Acoust. Soc. Am. 29 (6) (1957) 711–714, http://dx.doi.org/10.1121/1.1909021.
[6] G.B. Thurston, L.E. Hargrove, B.D. Cook, Nonlinear properties of circular orifices, J. Acoust. Soc. Am. 29 (9) (1957) 992–1001, http://dx.doi.org/10.1121/1.1914991.
[7] U. Ingard, H. Ising, Acoustic nonlinearity of an orifice, J. Acoust. Soc. Am. 42 (1) (1967) 6–17, http://dx.doi.org/10.1121/1.1910576.
[8] W.E. Zorumski, T.L. Parrott, Nonlinear Acoustic Theory for Rigid Porous Materials, Tech. Rep. NASA TN D-6196, NASA Tech. Note, 1971.
[9] A.S. Hersh, T. Rogers, Fluid Mechanical Model of the Acoustic Impedance of Small Orifices, Tech. Rep. NASA CR-2682, NASA Tech. Rep., 1976.
[10] A. Cummings, Transient and multiple frequency sound transmission through perforated plates at high amplitude, J. Acoust. Soc. Am. 79 (4) (1986) 942–951, http://dx.doi.org/10.1121/1.393691.
[11] X. Jing, X. Sun, Sound-excited flow and acoustic nonlinearity at an orifice, Phys. Fluids 14 (1) (2002) 268–276, http://dx.doi.org/10.1063/1.1423934.
[12] R.L. Panton, A.L. Goldman, Correlation of nonlinear orifice impedance, J. Acoust. Soc. Am. 60 (6) (1976) 1390–1396, http://dx.doi.org/10.1121/1.381232.
[13] G.B. Thurston, C.E. Martin Jr., Periodic fluid flow through circular orifices, J. Acoust. Soc. Am. 25 (1) (1953) 26–31, http://dx.doi.org/10.1121/1.1907003.
[14] P.G. Saffman, On the formation of vortex rings, Stud. Appl. Math. 54 (3) (1975) 261–268, http://dx.doi.org/10.1002/sapm1975543261.
[15] M. Peters, A. Hirschberg, Acoustically induced periodic vortex shedding at sharp edged open channel ends: Simple vortex models, J. Sound Vib. 161 (2) (1993) 281–299, http://dx.doi.org/10.1006/jsvi.1993.1072.
[16] R. Brandão, O. Schnitzer, Acoustic impedance of a cylindrical orifice, J. Fluid Mech. 892 (2020) A7, http://dx.doi.org/10.1017/jfm.2020.187.
[17] M. Howe, Acoustics of Fluid-Structure Interactions, Cambridge Monographs on Mechanics, Cambridge University Press, Cambridge, UK, 1998, http://dx.doi.org/10.1017/CBO9780511662898.
[18] H. Weber, Ueber die besselschen functionen und ihre anwendung auf die theorie der elektrischen ströme., J. Reine Angew. Math. 75 (1873) 75–105, URL http://eudml.org/doc/148193.
[19] M. Salikuddin, K. Ahuja, Acoustic power dissipation on radiation through duct terminations: Experiments, J. Sound Vib. 91 (4) (1983) 479–502, http://dx.doi.org/10.1016/0022-460X(83)90828-3.
[20] M. Howe, Attenuation of sound in a low mach number nozzle flow, J. Fluid Mech. 91 (2) (1979) 209–229, http://dx.doi.org/10.1017/S0022112079000124.
[21] M. Howe, The dissipation of sound at an edge, J. Sound Vib. 70 (3) (1980) 407–411, http://dx.doi.org/10.1016/0022-460X(80)90308-9.
[22] D. Bechert, Sound absorption caused by vorticity shedding, demonstrated with a jet flow, J. Sound Vib. 70 (3) (1980) 389–405, http://dx.doi.org/10.1016/0022-460X(80)90307-7.
[23] X. Jing, X. Sun, Discrete vortex simulation on the acoustic nonlinearity of an orifice, AIAA J. 38 (9) (2000) 1565–1572, http://dx.doi.org/10.2514/2.1178.
[24] B. Lyu, Analytical Green's function for the acoustic scattering by a flat plate with a serrated edge, J. Fluid Mech. 961 (2023) A33, http://dx.doi.org/10.1017/jfm.2023.256.
[25] M. Heckl, M. Howe, Stability analysis of the rijke tube with a Green's function approach, J. Sound Vib. 305 (4–5) (2007) 672–688, http://dx.doi.org/10.1016/j.jsv.2007.04.027.
[26] A. Bigongiari, M. Heckl, A Green's function approach to the rapid prediction of thermoacoustic instabilities in combustors, J. Fluid Mech. 798 (2016) 970–996, http://dx.doi.org/10.1017/jfm.2016.332.
[27] X. Wang, M. Heckl, 3-D thermoacoustic instability analysis based on Green's function approach, J. Sound Vib. 537 (2022) 116816, http://dx.doi.org/10.1016/j.jsv.2022.116816.
[28] A.K. Stoychev, T. Pedergnana, N. Noiray, Nonlinear acoustics of an aperture under grazing flow, Proc. R. Soc. A 480 (2283) (2024) 20230718, http://dx.doi.org/10.1098/rspa.2023.0718.
[29] J.D. Jackson, Classical Electrodynamics, third ed., Wiley, NJ 07030, USA, 1998.
[30] E. Titchmarsh, Introduction to the Theory of Fourier Integrals, Clarendon Press, Oxford, UK, 1948.
[31] D.N. Arnold, W.L. Wendland, The convergence of spline collocation for strongly elliptic equations on curves, Numer. Math. 47 (3) (1985) 317–341, http://dx.doi.org/10.1007/BF01389582.
[32] E.T. Copson, On the problem of the electrified disc, Proc. Ed. Math. Soc. 8 (1) (1947) 14–19, http://dx.doi.org/10.1017/S0013091500027644.
[33] D. Yang, A.S. Morgans, A semi-analytical model for the acoustic impedance of finite length circular holes with mean flow, J. Sound Vib. 384 (2016) 294–311, http://dx.doi.org/10.1016/j.jsv.2016.08.006.
[34] D. Yang, A.S. Morgans, The acoustics of short circular holes opening to confined and unconfined spaces, J. Sound Vib. 393 (2017) 41–61, http://dx.doi.org/10.1016/j.jsv.2016.12.027.
[35] K. Peat, R. Sugimoto, J. Horner, The effects of thickness on the impedance of a rectangular aperture in the presence of a grazing flow, J. Sound Vib. 292 (3) (2006) 610–625, http://dx.doi.org/10.1016/j.jsv.2005.08.012.
[36] P. Brokof, J. Guzmán-Iñigo, D. Yang, A.S. Morgans, The acoustics of short circular holes with reattached bias flow, J. Sound Vib. 546 (2023) 117435, http://dx.doi.org/10.1016/j.jsv.2022.117435.